



Non-destructive characterization of the spatial variation of γ/γ' lattice misfit in a single-crystal Ni-based superalloy by energy-resolved neutron imaging

Florencia Malamud,^{a,b,*} Javier Roberto Santisteban,^a Yan Gao,^c Takenao Shinohara,^d Kenichi Oikawa^d and Anton Tremsin^e

Received 13 July 2021

Accepted 5 January 2022

Edited by G. J. McIntyre, Australian Nuclear Science and Technology Organisation, Lucas Heights, Australia

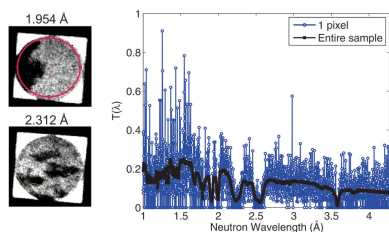
Keywords: Ni-based superalloys; energy-resolved neutron imaging; lattice misfit.

^aLaboratorio Argentino de Haces de Neutrones (LAHN), Comisión Nacional de Energía Atómica y CONICET, Avenida Bustillo 9500, San Carlos de Bariloche, Rio Negro, 8400, Argentina, ^bLaboratory for Neutron Scattering and Imaging, Paul Scherrer Institute, Forschungsstrasse 111, Villigen, 5232, Switzerland, ^cGeneral Electric Global Research Center, Niskayuna, NY 12309, USA, ^dJapan Atomic Energy Agency, Naka-gun Ibaraki 319-1195, Japan, and ^eSpace Sciences Laboratory, University of California at Berkeley, Berkeley, CA 94720, USA. *Correspondence e-mail: florencia.malamud@psi.ch

Lattice misfit in nickel-based superalloys is one of the important microstructural parameters that control their mechanical properties, such as creep behaviour at high temperatures. Here, energy-resolved neutron imaging experiments are performed at a spallation neutron source to determine the spatial variation of lattice misfit on a second-generation nickel-based single-crystal superalloy specimen produced from a failed low-cycle fatigue specimen. The wavelength spectrum of the neutrons scattered by the specimen displays a large number of peaks, each corresponding to a spot in traditional Laue diffraction experiments. An analysis of the position and width of those Laue peaks in the transmission spectra allows determination of the lattice parameters of the γ and γ' phases that compose the specimen, as well as the strain misfit and the misorientation between them. An analytical model is developed to describe the full wavelength pattern of Laue peaks arising from a specimen composed of two single crystals, and this model is used to perform least-squares refinements of the spectra measured at different positions of the specimen, with a spatial resolution of $\sim 500 \times 500 \mu\text{m}$. The local variations of the lattice parameter across the sample area were less than $4 \text{ m}\text{\AA}$ for both phases, and the lattice misfit remains essentially constant at a value of $0.30 \pm 0.03\%$, whilst the misorientation between the two phases is always smaller than $10'$. By contrast, the relative misorientation between different parts of the specimen varies locally up to 1.5° on a scale of millimetres.

1. Introduction

Owing to their good mechanical properties and corrosion resistance at elevated temperatures, nickel-based superalloys have been developed and improved over the past 50 years for several applications, such as gas turbine engines, aerospace and power generation (Stoloff *et al.*, 1987; Pollock & Tin, 2006; Donachie & Donachie, 2008; Reed *et al.*, 2009; Nowotnik, 2016). They are complex alloys composed of an ordered cubic phase (with space group $Pm\bar{3}m$ or $L1_2$, known as γ') and a disordered face-centred cubic (f.c.c.) phase (with space group $Fm\bar{3}m$, known as γ) (Long *et al.*, 2018). The high-temperature strength of nickel-based superalloys is due to the presence of the γ' phase, and therefore the size, volume fraction and distribution of γ' are key to control the creep strength (Nowotnik, 2016). The γ phase displays an f.c.c. crystal structure and forms the matrix in which the γ' phase precipitates with an ordered $L1_2$ structure. Both phases have a



cubic structure with similar lattice parameters. The γ' phase precipitates in a cube–cube orientation relationship with the f.c.c. phase, in the form of cuboids with coherent interfaces with the matrix (Long *et al.*, 2018). This cube–cube orientation means that the cell edges of the γ' phase are parallel to corresponding edges of the γ phase. The difference in lattice parameters between the two phases is defined by the misfit parameter δ (Long *et al.*, 2017):

$$\delta = 2 \frac{a_{\gamma'} - a_{\gamma}}{a_{\gamma'} + a_{\gamma}}, \quad (1)$$

where a_{γ} and $a_{\gamma'}$ are the lattice parameters of the γ and γ' phases, respectively, with positive misfit when γ' has a larger lattice parameter than γ . The amount of γ' and the misfit depend on the chemical composition of the phases (Pyczak *et al.*, 2004) and temperature (Huang *et al.*, 2018), and impact directly on the properties of the alloy (Caron & Khan, 1999; Pollock & Tin, 2006). The magnitude and the sign of the misfit also influence the evolution of the microstructure under stress at elevated temperatures (Dirand *et al.*, 2013; Long *et al.*, 2016). The misfit δ can be determined by X-ray diffraction (with laboratory or synchrotron sources) or neutron diffraction (Nathal *et al.*, 1985; Wu *et al.*, 2013; Long *et al.*, 2017; Luo *et al.*, 2018). In particular, for single-crystal nickel-based superalloys, the measurement of misfit can add additional complexity as compared with polycrystalline alloys (Huang *et al.*, 2018).

Neutron diffraction imaging (Woracek *et al.*, 2018) is a relatively novel technique that can provide information about the spatial variation of microstructure of crystalline materials. It has recently been applied to single-crystal superalloys to study the relationship between dendrite growth and mosaicity within a directionally solidified single-crystal turbine blade (Strickland *et al.*, 2020, 2021). Here, we use this technique to measure the misfit of a nickel-based superalloy single-crystal specimen, by performing time-of-flight (TOF) neutron

imaging experiments at a spallation neutron source. As has been demonstrated previously (Malamud & Santisteban, 2016), the neutron transmission spectrum of single-crystal materials is highly sensitive to the orientation of the crystal relative to the incoming beam and to the lattice parameter. Provided the neutron transmission spectrum can be measured in each pixel of the imaging data set, the angular misalignments and lattice mismatch can be mapped for the entire area of the sample. The fact that transmission spectra in imaging experiments are averaged through the entire sample thickness obviously introduces some limitations to this reconstruction. To demonstrate how sensitive this technique is to the angular misalignments within the sample, Fig. 1 shows three simulated neutron spectra for a single-crystal nickel-based superalloy sample with zero mosaicity. The intensity of the transmitted neutron beam changes substantially at certain wavelengths when the crystal is rotated. Consequently, if angular misalignments are present in a single-crystal sample, neutron transmission images taken at a specific wavelength will have different attenuations. Thus, not only can the location of large grains be revealed by these images but also the analysis of neutron spectra over a wide range of wavelengths can quantify the misalignment angles, as well as changes in the lattice parameters, for both phases in nickel-based superalloy materials, as demonstrated in this paper.

Interpretation of the contrast observed in the neutron images taken with different neutron wavelengths and the precise determination of lattice misfit required a thorough study of the wavelength spectrum of the neutrons scattered by the specimen. After such analysis, we have performed a least-squares full-pattern refinement of the wavelength spectra of the neutrons diffracted by the single crystal's planes, where the angles of crystal orientation and lattice parameters are fitted for both γ and γ' phases. To do this, we have extended a previous model of the neutron transmission by imperfect single crystals (Malamud & Santisteban, 2016), in order to

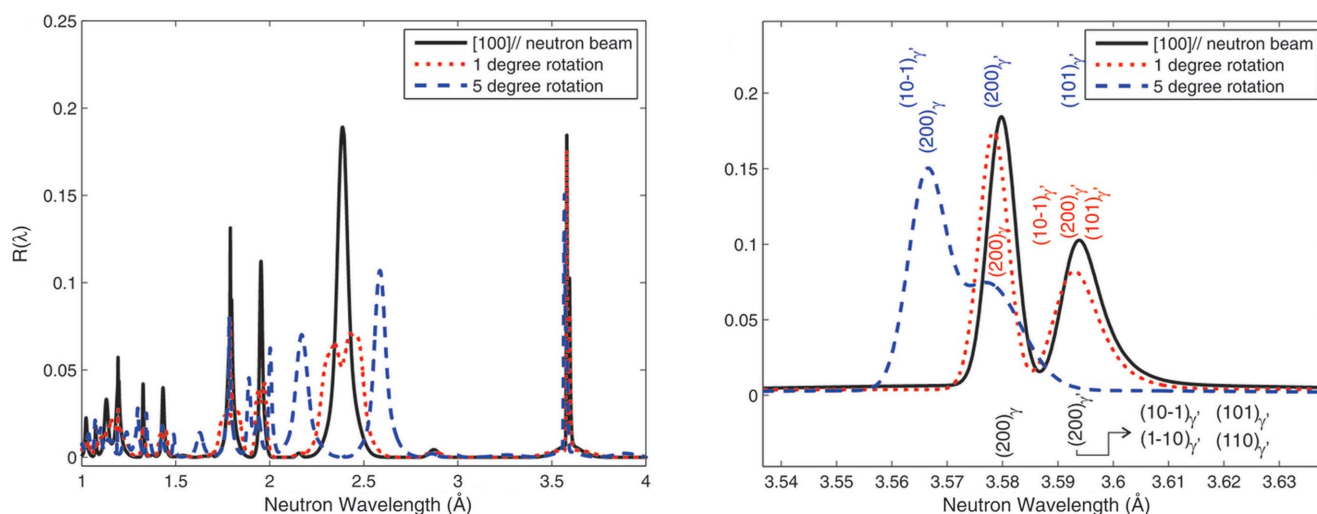


Figure 1

(a) Neutron spectra [complement to transmission as $R(\lambda) = 1 - T(\lambda)$] calculated for three sample orientations: (100) crystallographic plane is perfectly aligned with incoming neutron beam (solid line), and rotated by 1 and 5° (dotted and dashed lines, respectively). The scattering peaks corresponding to specific crystallographic planes are indexed in (b).

include materials composed of two monocrystalline phases. Provided with this model, we have obtained precise values of lattice parameters of the γ and γ' phases for different regions of the nickel-based superalloy specimen, together with additional crystallographic information, such as crystal misorientation between different regions, mosaicity and extinction factors.

2. Samples

The sample studied is a second-generation nickel-based single-crystal superalloy obtained from General Electric Research Center. The material is an experimental alloy, its composition consists of approximately 60 wt% Ni and Cr, Mo, Al, Ta and W in between 2 and 8 wt%, and it was grown in the [100] direction. A hold-time high-temperature low-cycle fatigue (LCF) test was applied in the [100] direction, and as a result, the γ' precipitates have fully deformed and the γ/γ' interfaces lost coherency. The sample used for the present tests was a 12 mm-long cylinder with 5 mm diameter produced from the gauge section of a failed LCF specimen, and the aim of this study was to explore the feasibility of determining lattice misfit by neutron imaging experiments. As the microstructure, including lattice misfit, is unique to the material's composition, thermal exposure history and deformation conditions, the misfit results obtained in the present study are not meant to be directly compared with those of similar alloys.

3. Experiments

Wavelength-resolved neutron imaging experiments on specimens at room temperature were performed at the Noboru imaging beamline, J-PARC Spallation Neutron Source, Japan (Harada *et al.*, 2014). At this facility, short pulses of neutrons are produced 25 times per second by the spallation process induced in a liquid-Hg target by periodic ~ 100 ns pulses of high-energy protons. Consequently, the energy of emitted neutrons is moderated through collisions within a liquid-hydrogen moderator. The width of the resulting neutron pulse is determined by this moderation process and is approximately a few tens of microseconds in the thermal and cold neutron ranges. Bursts of polychromatic neutrons emerge from the moderator and are transported and collimated into a beam that impacts on the specimen, placed in front of a neutron-counting detector, positioned at distance $L = 14.17$ m from the

source (Fig. 2). No neutron guides were installed in the beam, allowing a relatively uniform intensity of the beam. The collimation of the beam was determined by a pinhole aperture (positioned ~ 6.4 m from the detector) and was set to $L/D = 320:1$. The 2D detector is based on microchannel plates (MCPs) for conversion of neutrons into a charge of electrons registered by a Timepix readout (Tremisn & Vallergera, 2020) composed of a 512×512 array of pixels over an area of 28×28 mm. The unique MCPs in this detector were produced by Nova Scientific Inc. (Sturbridge, MA, USA) with their glass doped by ^{10}B and $^{\text{nat}}\text{Gd}$ atoms for detection of neutrons. The spatial resolution was determined by the pixel size ($55 \mu\text{m}$) of the detector. The position and time of arrival relative to the source trigger are measured for each neutron registered by the detector with an efficiency of $\sim 20\text{--}50\%$, depending on neutron energy. Although efficiency as high as 70% was achieved with this detection technology, a compromise between the number of activated pixels at the readout (to enable high counting rates) and the detector efficiency resulted in somewhat lower efficiency in this experiment. During the measurements, the sample was placed ~ 15 mm from the detector active area with its long axis along the direction of neutron propagation (Fig. 2). Since measured transmission spectra represent the integral values along the beam propagation, this sample orientation was chosen as corresponding to the largest single-crystal-like structure oriented along the neutron beam.

In the present experiments, the time resolution of neutron detection relative to the source trigger was set to $\sim 1 \mu\text{s}$. Images with and without the sample in place were collected for ~ 3000 TOF bins between 3500 and 15 296 μs . Hence, each image corresponds to a specific neutron wavelength in the range $[0.97\text{--}4.27] \text{ \AA}$, with a resolution of 0.0014 \AA . In principle, neutrons with longer wavelengths can be measured in the same experiment, but we limited our analysis to this wavelength range for two reasons: (i) the intensity of the neutron beam rapidly decreases beyond 4–5 \AA at this facility, reducing the signal-to-noise ratio in the measured spectra, and (ii) the number of TOF bins (images) was limited to ~ 3000 by the data acquisition software.

4. Data processing

Neutron transmission images at each wavelength $T(x, y, \lambda)$ are produced by computing the ratio between the images recorded with and without the specimen in the beam [$i(x, y, \lambda)$ and $i_0(x, y, \lambda)$, respectively], after correction for the dark signal when the beam is blocked [$b(x, y, \lambda)$]:

$$T(x, y, \lambda) = \frac{i(x, y, \lambda) - b(x, y, \lambda)}{i_0(x, y, \lambda) - b(x, y, \lambda)} \quad (2)$$

The transmission image provides microstructural characteristics about the material traversed by the neutron beam. This is because equation (2) removes the spectral variation of neutron beam intensity and eliminates any spatial variation or non-uniformities present in the incoming beam or in the detector. Fig. 3(a) displays $T(x, y, \lambda)$ images of the specimen

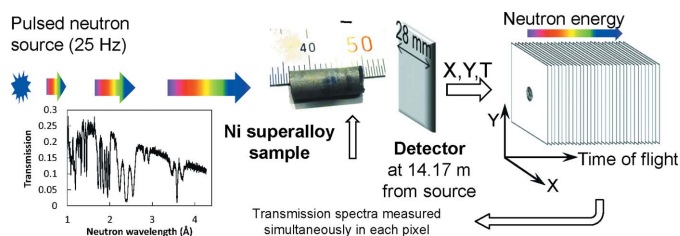


Figure 2
Schematic diagram of experimental setup used in energy-resolved neutron imaging (not to scale).

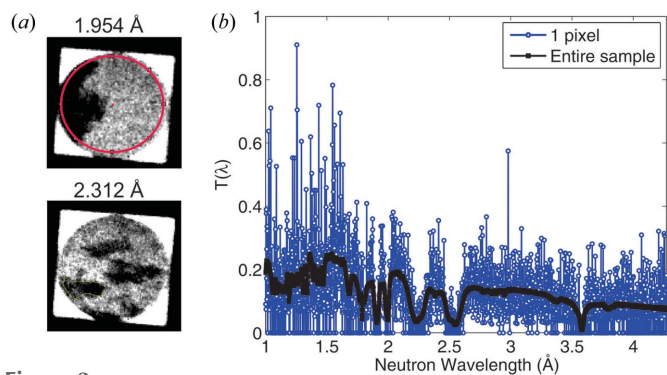


Figure 3
 (a) Neutron transmission images for different wavelengths. (b) Neutron spectra measured for a single pixel in the middle of sample (red dot) and for the entire specimen (red circle).

taken with neutrons of two different wavelengths, revealing clear variations across the specimen. The different attenuation levels reveal slight differences in the microstructure of the specimen along the path traversed by the neutron beam, due

to slight changes in crystalline orientation. The different contrast observed in each image results from the different sensitivities of the neutron wavelengths to variations in crystalline orientation.

More precise information about the specimen can be obtained from analysis of the transmitted spectra. However, compared with X-ray sources, neutron sources are relatively weak, so in energy-resolved neutron imaging experiments it is usually necessary to combine or ‘group’ the spectra registered by a number of adjacent pixels. In this sense there is always a compromise between the desired spatial resolution and the statistical quality of the spectra required by the analysis algorithms. Fig. 3(b) compares a spectrum recorded by a single pixel with that obtained by adding up the spectra recorded by all pixels within the area blocked by the specimen [the red circumference in Fig. 3(a)]. By choosing an appropriate grouping of pixels that provides an acceptable spatial resolution together with fair statistical quality for the corresponding spectra, it becomes possible to obtain precise, spatially resolved microstructural information from least-squares analysis of the individual spectra.

In order to understand the contrast displayed by the images, we have computed the transmitted spectra for some of the contrast regions in Fig. 3(a). The corresponding spectra are presented in Fig. 4, with the individual regions identified at the top of the figure.

As we are actually interested in the neutrons that have been removed from the incident beam by the specimen, the spectra are presented in terms of the complement of the transmission, $1 - T(\lambda)$. Region 1 corresponds to a region that is almost opaque to neutrons of $1.954 \pm 0.003 \text{ \AA}$ wavelength. Region 2 combines two smaller areas that are opaque to $2.175 \pm 0.003 \text{ \AA}$. Regions 3 and 4 are two small areas being relatively opaque to neutrons of wavelength 2.304 ± 0.003 and $2.312 \pm 0.003 \text{ \AA}$, respectively, and semi-transparent to the other wavelengths. All four spectra reveal a series of peaks, some of them appearing at the same positions in all of the spectra (e.g. the one at 3.6 \AA), whilst other peaks vary in position between the different regions. These peaks correspond to the neutrons diffracted out the beam by the different

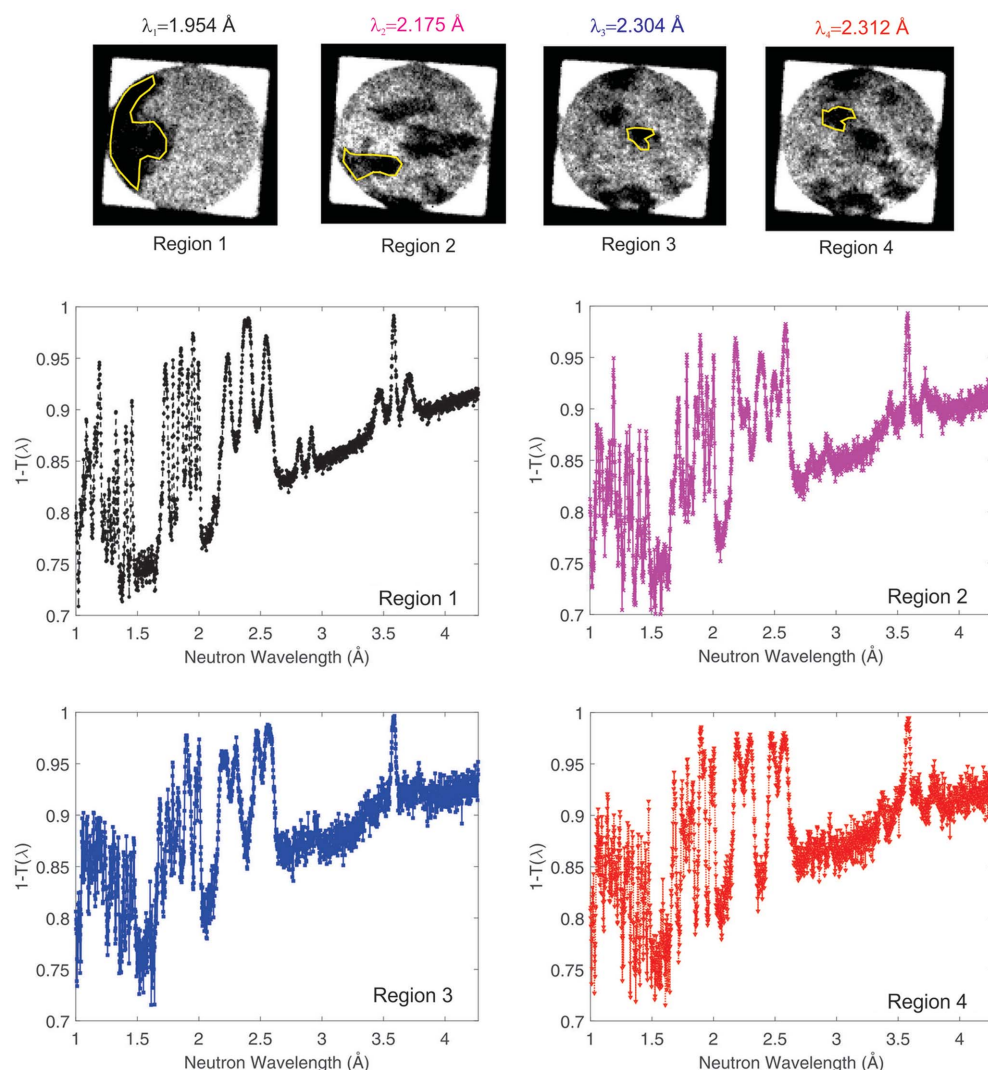


Figure 4
 Spectra of neutrons removed from the incident beam from different regions of the specimen.

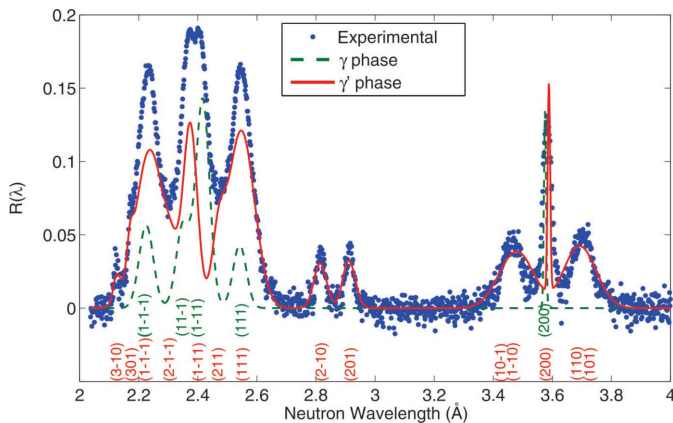


Figure 5
The experimental spectrum $R(\lambda)$ of Laue peaks for Region 1 (blue dots), together with the simulation of both phases' contributions $R(\lambda)^\gamma$ (dashed green line) and $R(\lambda)^{\gamma'}$ (red solid line). The same direction cosines, crystal mosaicity and mean-square microstrain were employed for both phases as initial guess parameters for the refinement.

crystallographic planes of the material (Santisteban, 2005). They are just a different representation of the spots observed in traditional Laue diffraction experiments, so we will refer to them as Laue peaks. The statistical quality achieved for the spectra shown in Fig. 4 is good enough to define the position, area and width of most peaks. The Laue peaks are on top of a rather smooth background, due to the combined effects of nuclear absorption and thermal diffuse scattering (Santisteban, 2005; Freund, 1983). In the analysis performed here we are only interested in the wavelength spectrum of Laue peaks, $R(\lambda)$, and hence this background will be subtracted from the $1 - T(\lambda)$ spectrum by approximating it with a polynomial function. An example of a typical $R(\lambda)$ spectrum is presented in Fig. 5.

5. Least-squares analysis of the full pattern of Laue peaks

The $R(\lambda)$ spectrum of Laue peaks constitutes a diffraction pattern that contains detailed microscopic information about the specimen. This information can be quantitatively extracted by performing a least-squares refinement of the experimental pattern, provided a sound physical model for $R(\lambda)$ is used. Such a full-pattern model for $R(\lambda)$ of a single mosaic crystal has been presented by Malamud & Santisteban (2016). Here we recall its basic ingredients and extend it to two crystals, in order to analyse the Laue peak spectra from the present nickel-based superalloy sample, composed of both γ and γ' single-crystal phases.

The spectrum $R(\lambda)$ of a single crystal is described by a series of Laue peaks resulting from all (hkl) planes meeting the diffraction conditions within the wavelength range of the experiment. Each Laue peak is characterized by its position λ_{hkl} , integrated area I_{hkl} and width ϖ_{hkl} (FWHM):

$$R(\lambda) = \sum_{hkl} I_{hkl} P(\lambda_{hkl}, \varpi_{hkl}, \lambda). \quad (3)$$

The function $P(\lambda_{hkl}, \varpi_{hkl}, \lambda)$ describes the actual peak shape (with unit area), dependent on the specific instrument. The position of the hkl Laue peak is given by the interplanar distance d_{hkl} and the angle α_{hkl} between the plane normal and the neutron beam:

$$\lambda_{hkl} = 2d_{hkl} \cos \alpha_{hkl}. \quad (4)$$

The peak width ϖ_{hkl} is a function of the crystal mosaicity and mean-square microstrain within the sample, the instrument resolution, and the angle α_{hkl} . The integrated intensity I_{hkl} is a complex function of the structure factor of the plane, the mosaicity, the beam divergence, and the geometry, size and orientation of the specimen. In the kinematical theory of diffraction for a thin crystal the peak area is directly given by the product of the attenuation coefficient for the reflection (μ_R^{hkl}) and the length of the path travelled by the neutron (l). The ratio between the actual area measured in the experiment and that predicted by the kinematical theory of diffraction is referred to here as the extinction factor (y_{hkl}), a value smaller than one. As a result, the Laue peak spectrum $R(\lambda)$ of an individual single crystal is written as

$$R(\lambda) = l \sum_{hkl} y_{hkl} \mu_R^{hkl} P(\lambda_{hkl}, \varpi_{hkl}, \lambda). \quad (5)$$

Considering the present nickel-based superalloy sample as being composed of two mosaic crystals (γ and γ'), and assuming no combined multiple reflections of neutrons on the crystalline planes of both γ and γ' phases, the observed $R(\lambda)$ can be modelled as a simple addition of the individual contributions:

$$R(\lambda) = R(\lambda)^\gamma + R(\lambda)^{\gamma'} = l^\gamma \sum_{hkl} y_{hkl}^\gamma \mu_{R,\gamma}^{hkl} P(\lambda_{hkl}^\gamma, \varpi_{hkl}^\gamma, \lambda) + l^{\gamma'} \sum_{hkl} y_{hkl}^{\gamma'} \mu_{R,\gamma'}^{hkl} P(\lambda_{hkl}^{\gamma'}, \varpi_{hkl}^{\gamma'}, \lambda). \quad (6)$$

Fig. 5 shows the experimental Laue peak spectrum $R(\lambda)$ for Region 1, together with the predicted $R(\lambda)^\gamma$ and $R(\lambda)^{\gamma'}$ spectra from lattice parameters a^γ and $a^{\gamma'}$ estimated from the literature (Nowotnik, 2016) and an appropriate crystal orientation, identical for both phases. The good agreement of the estimated positions and peaks of both phases and the experimental spectrum validates using equation (6) to describe the Laue peak spectra of the sample. In the estimation, the peak positions have been evaluated by a different expression for equation (4), in terms of the direction cosines of the incident beam (a_{11}, a_{12}, a_{13}) in the coordinate system of the crystal:

$$\lambda_{hkl}^\gamma = 2a^\gamma \frac{|ha_{11}^\gamma + ka_{12}^\gamma + la_{13}^\gamma|}{h^2 + k^2 + l^2},$$

$$\lambda_{hkl}^{\gamma'} = 2a^{\gamma'} \frac{|h'a_{11}^{\gamma'} + k'a_{12}^{\gamma'} + l'a_{13}^{\gamma'}|}{h'^2 + k'^2 + l'^2}. \quad (7)$$

The very different widths observed for Laue peaks found at similar wavelengths (e.g. at 3.6 and 3.7 Å) are due to the very different α_{hkl} angles for each reflection, as the peak width depends on $\tan \alpha_{hkl}$ (Santisteban, 2005). Narrow peaks correspond to back-reflected neutrons and broad peaks to forward-reflected neutrons. The detailed shape of the peaks

and the parameterization of the peak width are presented in Appendix A.

In this work we have implemented the full-pattern least-squares refinement of experimental neutron spectra of Laue peaks based on equation (6) into a MATLAB code. The numerical library has been specifically designed to analyse spatially resolved time-of-flight neutron transmission experiments in nickel-based superalloy single crystals performed at pulsed neutron sources. This Rietveld-type analysis provides precise values of the spatial variation of lattice parameters a^γ and $a^{\gamma'}$, which are used to define the misfit parameter δ . The input to the code is the experimental neutron transmission spectrum $T(\lambda)$, a set of parameters describing the instrument resolution, and initial guess values for the lattice parameters, crystal orientation, mosaicity and mean-square strain. The code extracts the $R(\lambda)$ spectrum of Laue peaks from the $[1 - T(\lambda)]$ spectrum by subtracting an absorption/diffuse scattering contribution, which is approximated by a fifth-degree polynomial baseline fit on the experimental data. The Laue peaks are indexed using an implementation of the method described in Appendix A of the article by Santisteban (2005). After indexing, a full-pattern least-squares refinement of all peaks within the selected wavelength range is performed on the experimental $R(\lambda)$ spectrum, using the lattice parameters a^γ and $a^{\gamma'}$, the direction cosines a_{11}^γ , a_{12}^γ , $a_{11}^{\gamma'}$ and $a_{12}^{\gamma'}$, the mean-square strains ε^γ and $\varepsilon^{\gamma'}$, the mosaicities η^γ and $\eta^{\gamma'}$, and the peak area parameters A_{hkl}^γ and $A_{h'k'l'}^{\gamma'}$. The direction cosines of the incident beam should in principle be the same for both phases since the γ' phase precipitates in a cube–cube coherent orientation with the γ matrix. However, as slight deviations may exist, the direction cosines of both phases can be refined independently, hence allowing determination of the misorientation between the two phases.

Fig. 6 shows the experimental $R(\lambda)$ spectrum for Region 1 together with the refined pattern of Laue peaks and their corresponding indexing, although some Miller indices have been omitted for clarity. The very good agreement between the two curves demonstrates the capability of the proposed model to describe the Laue peak spectra of nickel-based superalloys. The goodness of the refinements has been quantified by means of the parameter G , which estimates the

agreement between the observed and calculated $R(\lambda)$ profiles, defined as

$$G = 100 \frac{\sum_i |y_i(\text{obs}) - y_i(\text{cal})|}{(N_{\text{obs}} - N_p)}, \quad (8)$$

where $y_i(\text{obs})$ is the observed intensity at the i th wavelength interval, $y_i(\text{cal})$ the calculated intensity, N_{obs} the number of observations and N_p the number of fitting parameters.

6. Results

The spectra of Laue peaks corresponding to Regions 1–4 were analysed using the full-pattern analysis described in the previous section. In order to analyse the reproducibility of the fitted microstructural parameters, the routine was applied using different wavelength ranges: [1–4] Å, [1.6–4] Å and [2–4] Å, containing 46 and 136, 14 and 43, and 5 and 22 Laue peaks of the γ and γ' phases, respectively. The black solid line in Fig. 6 shows the result of such refinement for Region 1 for the [1–4] Å wavelength range, where the peaks of both γ and γ' phases have been clearly indexed (in green and red, respectively). As can be appreciated from the difference curve shown at the bottom, the fitting is very good with a G parameter of 1.2%, even for the shorter-wavelength range where the peaks of the two phases are highly superimposed.

The refined values of the lattice parameter for each phase and the corresponding misfit are listed in Table 1, together with the mean value of the G parameter obtained for each area. The uncertainties presented in Table 1 correspond to the standard deviation of the lattice parameter refined from the different wavelength ranges for the same area.

The misorientation between the two phases $\gamma \angle \gamma'$ and the misalignment between the different regions reported in Table 1 were evaluated from the refined direction cosines a_{11}^γ , a_{12}^γ , $a_{11}^{\gamma'}$ and $a_{12}^{\gamma'}$ of the incident neutron beam in the coordinate system of the crystal. The misalignment of the different regions relative to Region 1 is given in the plane that contains the incident and reflected neutron beams. For each region, the misorientation between the γ and γ' phases is less than 10° . On the other hand, the misalignment between different areas

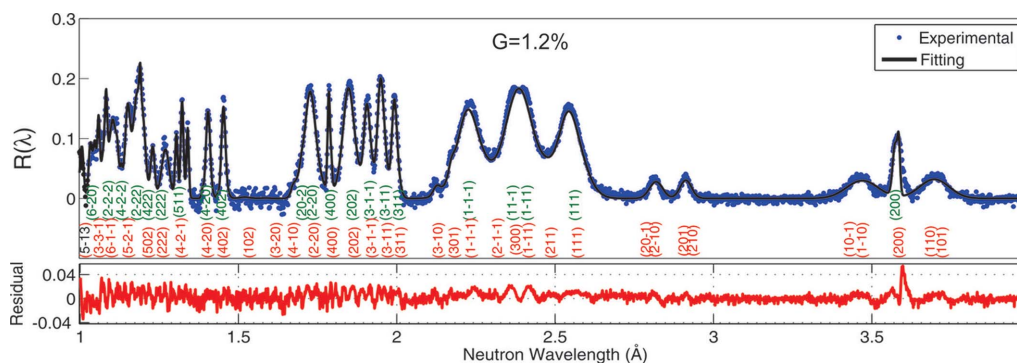


Figure 6

The experimental spectrum $R(\lambda)$ of Laue peaks for Region 1 (blue dots) together with the results of the full-pattern least-squares refinement performed within the [1–4] Å wavelength range (solid black line) and the corresponding residual (solid red line). Most of the peaks of the γ (green labels) and γ' (red labels) phases are indexed, but for clarity some minor peaks have been omitted.

Table 1

Refined values of the lattice parameter and the corresponding misfit measured for areas 1–4 and each phase, together with the mean value of the G parameter, the misorientation between phases and the misalignment between the different regions relative to Region 1.

Area	Lattice parameter		Misfit	Misorientation		G (%)
	a' (Å)	a'' (Å)	δ (%)†	$\gamma \angle \gamma'$ (°)	\angle area 1 (°)	
1	3.5802 (3)	3.5918 (8)	0.32 (2)	0.05	–	1.2
2	3.5798 (4)	3.5909 (9)	0.31 (3)	0.07	1.05	1.5
3	3.5807 (2)	3.5908 (6)	0.29 (3)	0.15	1.90	1.8
4	3.5790 (7)	3.5903 (4)	0.32 (2)	0.12	1.91	1.8

† $\delta = 2(a' - a'') / (a' + a'')$.

across the sample, measured with respect to Region 1, is approximately 1° for Region 2 and less than 2° for Regions 3 and 4. This misorientation shifts the peaks of both phases and is responsible for the most noticeable changes observed in the spectra of the different regions (Fig. 4). A detailed analysis of this effect is shown in Fig. 7, where the experimental spectra $R(\lambda)$ of the Laue peaks and the results of the full-pattern least-squares refinement performed on the [1–4] Å wavelength range are displayed for the region within the [1.5–2.7] Å wavelength range.

As is shown in Fig. 7, for Region 1 the intensity of the Bragg-reflected component around $\lambda_1 = 1.95$ Å is higher (0.2) than the corresponding value for Region 2 (0.15), while for Regions 3 and 4 $R(\lambda)$ is less than 0.05. These differences in the Bragg-reflected component values around λ_1 are related to the

movement of the $3\bar{1}1$ reflection. For $\lambda_2 = 2.175$ Å, the highest intensity of $R(\lambda)$ corresponds to Region 2 (0.17), followed by Regions 3 and 4 (0.13) and Region 1 (0.07), associated with the position of the 301 and 310 reflections. On the other hand, for $\lambda_3 = 2.304$ Å and $\lambda_4 = 2.312$ Å, Regions 3 and 4 display similar $R(\lambda)$ values (0.13), while Regions 1 and 2 correspond to lower intensity (0.08), correlated with the shift of the 111 and $1\bar{1}1$ reflections. All the peak shifts are related to the misorientation between regions in the plane that contains the incident and reflected beams, and that is the reason for the different transmission values and, therefore, the different grey levels displayed in Fig. 4.

Note that Region 1 and Region 2 overlap, even though they present differences on their transmission spectra due to their degree of misalignment. This intersection is clearly displayed in Fig. 8, where Region 1 is represented with vertical stripes and Region 2 with horizontal lines. In order to study in detail the variation of the crystalline orientation and lattice misfit within both regions, we have extracted the transmitted wavelength spectra from selected small areas of 10×10 pixels ($\sim 550 \times 550$ μm) inside Region 1 (A and B), at the intersection of Region 1 and Region 2 (C), inside Region 2 (D), and outside both areas (E and F), as shown in Fig. 8. The experimental Bragg-reflected components of areas A–F were analysed using the full-pattern analysis, employing the same refinement strategy as for Regions 1 and 2. Fig. 8 shows the least-squares refinement results performed on the [1–4] Å wavelength range for each area within the [1.5–2.7] Å

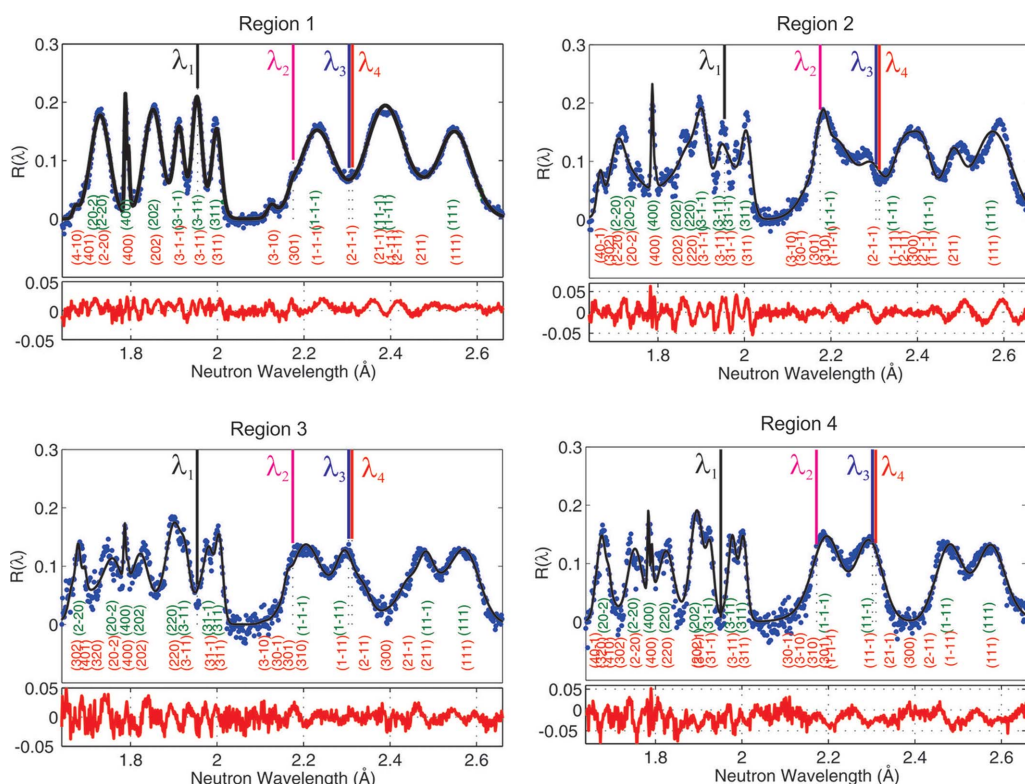


Figure 7

The experimental Bragg-scattered component $R(\lambda)$ (blue dots), the results of the full-pattern least-squares refinement (solid black lines) and the corresponding residual (solid red lines), for different regions for the [1.5–2.7] Å wavelength range.

Table 2

Refined values of the lattice parameter for each phase and for areas A–F, the corresponding misfit, the misorientation between phases $\gamma \angle \gamma'$, and the misalignment between the different regions, relative to Region 1 (\angle area 1) and area A (\angle area A).

Area	Lattice parameter		Misfit δ (%)†	Misorientation			<i>G</i> (%)
	a' (Å)	a'' (Å)		$\gamma \angle \gamma'$ (min)	\angle area 1 (°)	\angle area A (°)	
A	3.5802 (3)	3.5911 (7)	0.30 (1)	10	0.2	–	2.1
B	3.5803 (4)	3.5910 (5)	0.30 (2)	3	0.3	0.2	2.7
C	3.5798 (4)	3.5899 (9)	0.28 (3)	11	0.9	1.0	3.1
D	3.5808 (9)	3.5911 (8)	0.29 (4)	8	1.2	1.3	2.9
E	3.5814 (4)	3.5926 (10)	0.31 (3)	5	1.8	1.6	2.7
F	3.5796 (6)	3.5896 (5)	0.28 (4)	9	2.2	2.0	2.0

† $\delta = 2(a'' - a') / (a' + a'')$.

wavelength range, presenting an excellent agreement with the experimental $R(\lambda)$ pattern for all regions.

The refined values of the lattice parameter for each phase within each region, the corresponding misfit, the misorientation between the two phases $\gamma \angle \gamma'$, and the misalignment between the different regions relative to Region 1 (\angle area 1) and to area A (\angle area A) are listed in Table 2, together with the mean value of the *G* parameter. As before, the uncer-

tainties of the lattice parameters correspond to the standard deviation of the refined parameters from the different wavelength ranges and uncertainties of the misfit values are calculated by error propagation from those values. As expected, owing to the lower neutron statistics for the small areas, the *G* values are slightly higher than in the previous cases presented in Table 1. The calculated misfit from the refined lattice parameters for both phases is $\sim 0.3\%$ for all areas and the misorientation between the two phases is approximately $10'$. The misalignment measured with respect to Region 1 is less than 1° for the areas inside Region 1 (A, B), approximately 1° at the intersection of Region 1 and Region 2 (C), 1.2° for area D (within Region 2), and higher than 1.8° for the areas outside Regions 1 and 2 (E and F). On the other hand, the misorientation with respect to area A is 0.2° for area B, approximately 1° for C and D, and higher than 1.5° for the selected areas outside Regions 1 and 2.

7. Discussion

We have performed wavelength-resolved neutron imaging experiments on a second-generation nickel-based single-crystal superalloy sample from a failed low-cycle fatigue

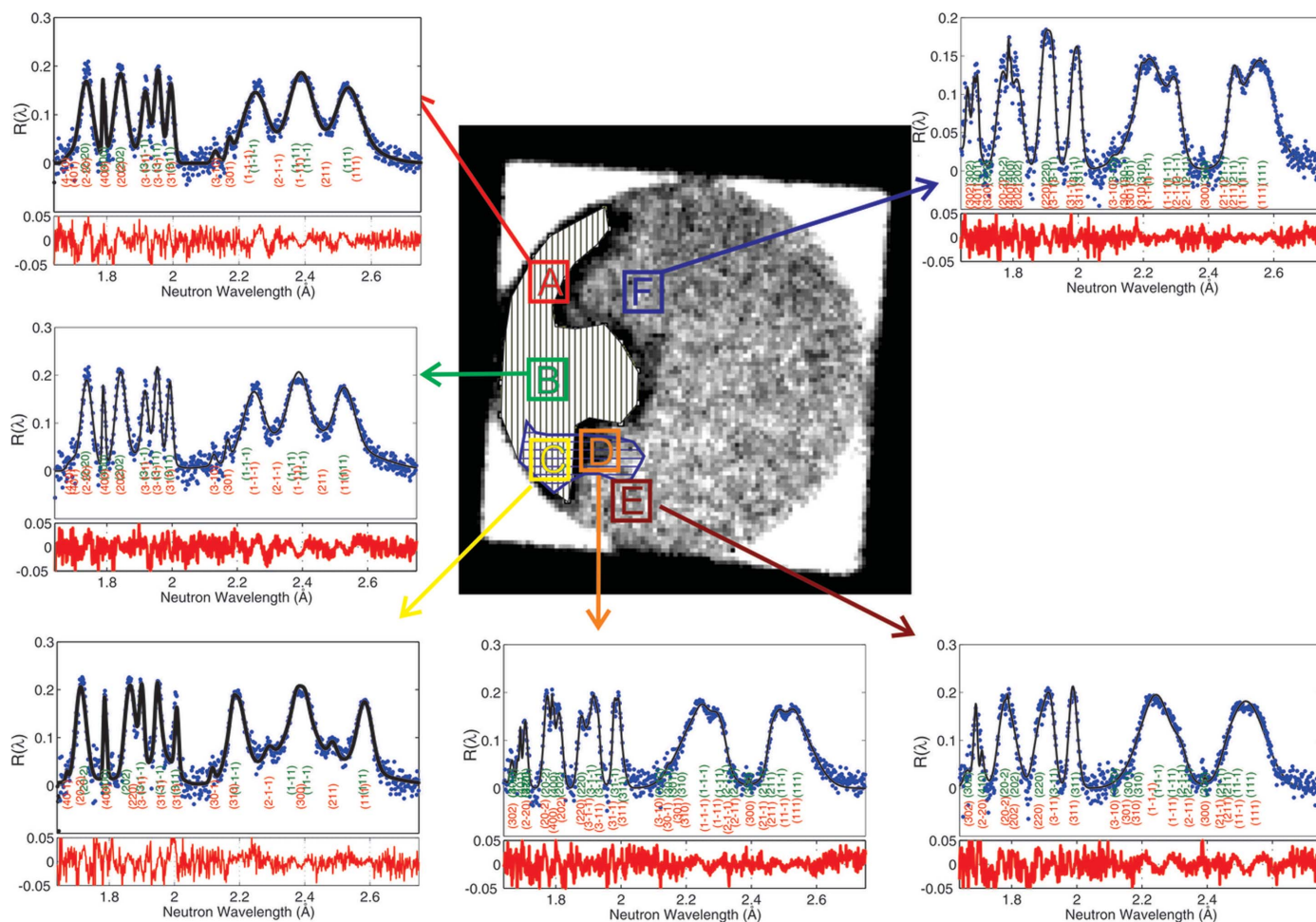


Figure 8

The experimental Bragg-scattered component $R(\lambda)$ (blue dots) for areas A to F, the results of the full pattern least-squares refinement (solid black lines) and the corresponding residuals (solid red lines).

specimen. The transmission images at particular wavelengths display different attenuations, as seen in Fig. 4, which reveal subtle differences in the microstructure of the specimen. The analysis performed here has shown that the different contrasts observed in each image result almost exclusively from local variations in the orientation of this dual-phase single-crystal material. This is because the variation in neutron attenuation observed for different wavelengths results from neutrons that are reflected by the crystal planes into the Laue spots commonly observed by traditional Laue diffraction. The neutrons removed from the beam into a specific Laue spot are identified by the Miller indices (hkl) of the reflecting plane and the angle α_{hkl} between the plane normal and neutron beam. Their wavelength λ_{hkl} and their wavelength spread are both highly dependent on this angle (by the cosine and tangent, respectively). So the neutron attenuation images taken with wavelengths near a particular λ_{hkl} are very sensitive to small misorientation of the single crystal.

The neutron attenuation is sensitive to the misorientation of a single-crystal material around the axis perpendicular to the plane that contains the incident beam and Laue-reflected neutron beam, but it is insensitive to rotations around the direction of the \mathbf{q} (diffraction scattering) vector. This explains the observation that in the $R(\lambda)$ spectra measured for the different contrast regions some peaks appear consistently at the same position in all regions, whilst others were clearly varying between the different regions.

The full-pattern analysis of the positions and widths of all the Laue peaks appearing in the wavelength spectra $R(\lambda)$ for the different contrast areas of Figs. 4 and 8 provided the lattice parameter and the misorientation of both γ and γ' phases for the material within each region, as listed in Tables 1 and 2, respectively. This was done by performing a least-squares refinement of the experimental data with a sound physical model. As is shown in Figs. 6, 7 and 8, the Bragg-scattered component $R(\lambda)$ is well described by the full-pattern model presented in equation (6), as a simple addition of the contributions from the individual mosaic crystal of both γ and γ' phases.

The residual plots of Fig. 7, 8 and 9 show that the full-pattern analysis provides an excellent agreement with the experimental $R(\lambda)$ pattern for all regions, for areas as small as $550 \times 550 \mu\text{m}$, even in the short-wavelength range where Bragg peaks are highly superimposed. This good agreement is quantified by the reported values of the parameter G in Tables 1 and 2, always in the range (1–3)% which is close to the standard deviation of the experimental data. The refined parameters show little dependence on the wavelength range employed to perform the fitting, owing to the high number of reflections of both phases included within each wavelength interval. In the present analysis, we have adopted the criteria of taking the standard deviation of the parameters obtained from the refinements performed at different wavelength ranges as a measure of the uncertainty of the reported lattice parameters.

The values reported in Tables 1 and 2 show that the misfit remains essentially constant among different regions and different areas with values of approximately 0.3%. The orientation relationship between the γ and γ' phases is nearly perfect (misorientation less than $10'$), as obtained from the refined direction cosines a_{11}^{γ} , a_{12}^{γ} , $a_{11}^{\gamma'}$ and $a_{12}^{\gamma'}$ of the incident neutron beam in the coordinate system of the crystal.

We recall that the proposed full-pattern model leaves the areas of the peak as unconstrained, free fitting parameters. This means that in the present formulation we do not intend to describe the extinction process or extract quantitative information about the volume of the γ and γ' phases. An analytical model for the areas of the Laue peaks capable of efficient least-squares analysis could follow the ideas of the formulation presented by Dessieux *et al.* (2018).

In the present experimental arrangement, the individual Laue peaks from the γ and γ' phases can never be resolved separately (as observed in Figs. 6, 7 and 8), yet we are able to obtain lattice parameters and the misfit strain and misorientation between the phases. The qualitative explanation for this is presented in Fig. 9, which shows details of the contribution of each phase $R(\lambda)^{\gamma}$ (dashed green line) and $R(\lambda)^{\gamma'}$ (red solid line) to the total refined spectrum presented in Fig. 6,

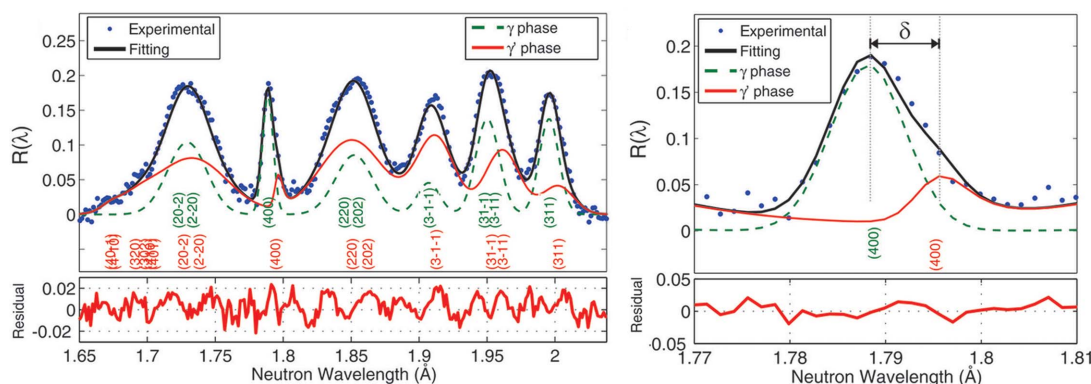


Figure 9 (a) The experimental Bragg-scattered component $R(\lambda)$ for Region 1 (blue dots) and the full-pattern least-squares refinement (solid black line) within the [1.65–2.03] Å wavelength range showing both phases' refined contributions $R(\lambda)^{\gamma}$ (dashed green line) and $R(\lambda)^{\gamma'}$ (red solid line). (b) Detail of the 400 peaks

corresponding to Region 1. The highest resolution in peak position is obtained for those Laue peaks whose plane normal is nearly parallel to the incident beam, which in the present case corresponds to the 200 and 400 peaks. As observed in Fig. 9(b), explaining the asymmetry and width of the peak appearing at 1.79 Å requires including the contributions from both phases [(400) γ and (400) γ'], e.g. the presence of the γ' phase manifests as a shoulder on the larger (400) γ phase peak. Hence, under the assumption that both phases always share the same orientation, it is in principle possible to define the positions of both the (400) γ and (400) γ' peaks and define the misfit parameter simply by

$$\delta = 2 \frac{\lambda_{400}^{\gamma'} - \lambda_{400}^{\gamma}}{\lambda_{400}^{\gamma'} + \lambda_{400}^{\gamma}}. \quad (9)$$

Employing this approach, the misfit parameters for Regions 1, 2, 3 and 4 are 0.31, 0.33, 0.30 and 0.31%, respectively, which are consistent with the values presented in Table 1. Although much simpler, this approach has benefited from information provided by the full-pattern analysis in terms of the indexing of the peaks, the misorientation between the phases, and the definition of the width of both peaks through the functional dependence on wavelength and orientation explained in Appendix A. Hence, once such information about the sample and experimental arrangement is known, the spatial distribution of the misfit parameter could be defined by simply refining the two overlapping Laue peaks whose plane normals are aligned to the incident neutron beam direction

Fig. 9(a) shows that the refined Laue peaks from the γ' phase are consistently wider than those from the γ phase. This observation also reveals information about the microstructure of the phases, which can be extracted from the refined parameters. The model for the width $v_{hkl}(\lambda)$ of the Laue peaks is given by equation (15) of Appendix A. It includes a contribution from the uncertainty in the α_{hkl} angle (given by the convolution of the incident beam divergence ϱ and the single-crystal mosaicity η), the uncertainty in the interplanar distance d_{hkl} between the reflecting planes (quantified by the mean-square elastic deformation of the crystal structure ε), and the uncertainty on the measured time of flight of the neutrons (defined by the neutron moderator and total flight path of the neutrons). The refined values of the overall mosaicity η for the γ' phase ([21–26]') were nearly double those for the γ phase ([44–53]'). This can be interpreted as a measure of the rafting and plastic deformation introduced in the γ' phase during the LFC tests.

On the other hand, as seen in Table 1, the misalignment between Region 1 and Region 2 is approximately 1°, while the misorientation between Region 1 and Regions 3 and 4 is almost 2°. Those results are consistent with the misorientation defined from the transmission signals extracted for small areas (~550 × 550 μm) within, outside and at the intersection of Region 1 and Region 2. In this case, the misalignment measured with respect to Region 1 is less than 1° for A, B and C, 1.2° for area D, and ~2° for E and F, while the misorientation measured with respect to section A is 0.2° for area B,

~1° for C and D, and higher than 1.5° for E and F. Since this misalignment produces different attenuations observed in the images of Fig. 4 for each neutron wavelength, these results show that by using energy-selective neutron imaging it is possible to identify regions misoriented by ~1° with respect to each other.

The analysis of misfit strain and misorientation performed here has been applied using a pixel size of ~500 × 500 μm, but it can in principle be applied using smaller pixels for higher spatial resolution.

8. Conclusions

The neutron transmission images of a 12 mm-thick sample of a second-generation nickel-based single-crystal superalloy produced from a failed low-cycle fatigue specimen showed clear patterns which changed markedly for images taken with different neutron wavelengths. The patterns were due to spatial differences in the microstructure of the specimen along the neutron beam direction.

Analysis of the wavelength spectrum of the neutrons scattered by the specimen revealed a series of peaks at specific neutron wavelengths, due to Laue diffraction from the crystal planes of the two monocrystalline phases, γ and γ' . The lattice parameters and crystalline orientation of the two phases, and the misorientations and lattice misfit between them, were determined from the positions of those Laue peaks in the wavelength spectra. The lattice parameters and orientations were obtained from a full-pattern least-squares refinement using a two-phase model specifically introduced in this paper, after extending a single-phase model presented elsewhere (Malamud & Santisteban, 2016).

The results showed that the lattice parameters of both phases (3.579–3.582 Å for the γ phase and 3.589–3.593 Å for the γ' phase), as well as their relative misfit (~0.3%) and misorientation (<10'), remain fairly constant across the specimen, but the macroscopic orientation of the crystal lattice rotated by as much as 1.5°. This univocally showed that the patterns observed in the monochromatic images were due to local changes in the crystalline orientation of the two-phase material. This could result from the plastic deformation occurring during the mechanical test or may have been already present in the specimen as a result of the manufacturing process.

This study shows that energy-resolved neutron imaging can be used to non-destructively characterize the microstructure of nickel-based superalloys, by providing maps of the spatial distribution of lattice parameters, misfit and misorientations of the γ and γ' phases in the crystal with a spatial resolution of ~500 × 500 μm.

APPENDIX A

Full-pattern analysis of mosaic crystals

The experimental Bragg-reflected spectrum $R(\lambda)$ of mosaic crystals consists of a collection of individual peaks, each

described by their position (λ_{hkl}), width (ϖ_{hkl}) and an integrated area (I_{hkl}). In another work (Malamud & Santisteban, 2016), we have developed a full-pattern least-squares analysis of the experimental $R(\lambda)$ by implementing a physically based analytical expression of equation (3). Below we provide the analytical expressions of peak shape $P(\lambda_{hkl}, \varpi_{hkl}, \lambda)$, peak position λ_{hkl} and peak broadening ϖ_{hkl} adopted in the present analysis.

Integrated intensity. Within the kinematic theory of diffraction, the integrated intensity of the hkl peak is given by $I_{hkl} = 1 - \exp(-l\mu_R^{hkl})$, where l is the crystal thicknesses in the neutron beam direction and μ_R^{hkl} is the integrated reflectivity of the hkl reflection (Zachariasen, 1945).

$$\mu_R^{hkl} = \frac{|F_{hkl}|^2 \lambda_{hkl}^4}{2V^2 \sin^2 \theta_{hkl}}, \quad (10)$$

where $|F_{hkl}|$ is the structure factor (including the Debye-Waller factor), V is the volume of the unit cell and $\theta_{hkl} = \sin^{-1}[\lambda_{hkl}/(2d_{hkl})]$ is the Bragg angle for the reflection. In particular, for a thin specimen ($l \ll 1/\mu_R^{hkl}$) the integrated intensity becomes $I_{hkl} \simeq l\mu_R^{hkl}$. Since in practice the integrated intensity is smaller than the area predicted by the kinematical theory due to the extinction of the neutron beam (Bacon & Lowde, 1948; Zachariasen, 1969), we have included in the model an extinction factor y_{hkl} , representing the ratio between the integrated area predicted by the kinematical theory and the actual value measured by the experiment:

$$R(\lambda) = l \sum_{hkl} y_{hkl} \mu_R^{hkl} P(\lambda_{hkl}, \varpi_{hkl}, \lambda). \quad (11)$$

Peak profile. The peak profile function $P(\lambda_{hkl}, \varpi_{hkl}, \lambda)$ is defined by the instrumental resolution function, which is typically asymmetric in TOF experiments performed at accelerator-based neutron sources. Here, we adopt for the resolution function the model proposed by Kropff *et al.* (1982), which represents the geometrical deviations by a Gaussian of deviation $v_{hkl}(\lambda)$ and uses a truncated decaying exponential of constant $\tau_{hkl}(\lambda)$ to describe the uncertainty of the emission time of the neutron. The expression for a peak located at wavelength λ_{hkl} is

$$\begin{aligned} P(\lambda_{hkl}, [\tau_{hkl}, v_{hkl}], \lambda) &= \frac{1}{\tau_{hkl}(\lambda)} \exp\left[-\frac{\lambda - \lambda_{hkl}}{\tau_{hkl}(\lambda)}\right] \\ &\quad \otimes \frac{1}{(2\pi)^{1/2} v_{hkl}(\lambda)} \exp\left[-\frac{(\lambda - \lambda_{hkl})^2}{2 v_{hkl}(\lambda)^2}\right] \\ &= \frac{1}{2\tau_{hkl}(\lambda)} \exp\left[-\frac{\lambda - \lambda_{hkl}}{\tau_{hkl}(\lambda)} + \frac{v_{hkl}(\lambda)^2}{2\tau_{hkl}(\lambda)^2}\right] \\ &\quad \times \operatorname{erfc}\left[-\frac{\lambda - \lambda_{hkl}}{2^{1/2} v_{hkl}(\lambda)} + \frac{v_{hkl}(\lambda)}{\tau_{hkl}(\lambda)}\right]. \quad (12) \end{aligned}$$

In this peak shape, the FWHM ϖ_{hkl} displays a complex analytical expression as a function of v_{hkl} , τ_{hkl} and λ_{hkl} .

Peak position. The position of the peaks depends on the orientation between the incident beam and the crystal, specified by Bragg's law:

$$\lambda_{hkl} = 2d_{hkl} \cos \alpha_{hkl}, \quad (13)$$

where d_{hkl} is the interplanar distance for the (hkl) planes and α_{hkl} is the angle between the neutron beam and the normal to the reflecting crystal planes. For a cubic crystal with lattice parameter a , the hkl reflection diffracts neutrons of wavelength

$$\lambda_{hkl} = 2a \frac{|ha_{11} + ka_{12} + la_{13}|}{h^2 + k^2 + l^2}, \quad (14)$$

where a_{11} , a_{12} and a_{13} are the direction cosines of the incident neutron beam in the coordinate system of the crystal, related by the normalization condition $a_{11}^2 + a_{12}^2 + a_{13}^2 = 1$.

Peak width. The main contribution to the width $v_{hkl}(\lambda)$ of the Gaussian component of the instrument resolution comes from the uncertainty in the neutron wavelength $\Delta\lambda_{hkl}$ of the reflected neutrons. In the present model $v_{hkl}(\lambda)$ is given by

$$v_{hkl}(\lambda)^2 = \lambda_{hkl}^2 [\varepsilon^2 + (\varrho^2 + \eta^2) \tan^2 \alpha_{hkl}], \quad (15)$$

where $\overline{\varepsilon^2} = (\Delta d_{hkl}/d_{hkl})^2$ represents the mean-square elastic deformation of the crystal structure. ϱ and η represent the Gaussian distribution widths of the incident beam divergence and the crystal mosaic blocks, respectively. In particular, the mosaicity η gives a measure of the misorientation of the composing crystal blocks. On the other hand, the asymmetric contribution to the peak width does not involve crystallographic effects but depends on the specific hkl reflection through the neutron wavelength:

$$\tau_{hkl} = \tau(\lambda = \lambda_{hkl}). \quad (16)$$

The function $\tau(\lambda)$ is a characteristic of the moderator, and it has a smooth dependence on neutron wavelength, reaching a plateau at long wavelengths (Kropff *et al.*, 1982).

Acknowledgements

The authors acknowledge access to the neutron imaging beamline Noboru at the Materials and Life Sciences Facility (JPARC, Japan) and the great help of our colleagues at this facility. The readout electronics used in the experiments were developed within the Medipix collaboration with help from the collaboration members, especially from the Czech Technical University in Prague, Advacam (Czech Republic and Finland) and NiKHEF (Netherlands).

Funding information

The work on the development of energy-resolved imaging at the University of California was partially funded through the research grants by the United States Department of Energy (DOE) under contract No. DE-AC02-05CH11231. The data analysis work was partially funded by the Argentine grant ANPCYT PICT 2017-2547.

References

- Bacon, G. E. & Lowde, R. D. (1948). *Acta Cryst.* **1**, 303–314.
- Caron, P. & Khan, T. (1999). *Aerosp. Sci. Technol.* **3**, 513–523.
- Dessieux, L. L., Stoica, A. D. & Bingham, P. R. (2018). *Rev. Sci. Instrum.* **89**, 025103.

- Dirand, L., Cormier, J., Jacques, A., Chateau-Cornu, J.-P., Schenk, T., Ferry, O. & Bastie, P. (2013). *Mater. Charact.* **77**, 32–46.
- Donachie, M. J. & Donachie, S. J. (2008). *Superalloys: a Technical Guide*. Materials Park: ASM.
- Freund, A. K. (1983). *Nucl. Instrum. Methods Phys. Res.* **213**, 495–501.
- Harada, M., Oikawa, K., Ooi, M., Kai, T., Shinohara, T., Sakai, K. & Maekawa, F. (2014). *JPS Conf. Proc.* **1**, 014015.
- Huang, S., An, K., Gao, Y. & Suzuki, A. (2018). *Metall. Mater. Trans. A*, **49**, 740–751.
- Kropff, F., Granada, J. R. & Mayer, R. E. (1982). *Nucl. Instrum. Methods Phys. Res.* **198**, 515–521.
- Long, H., Mao, S., Liu, Y., Zhang, Z. & Han, X. (2018). *J. Alloys Compd.* **743**, 203–220.
- Long, H., Mao, S., Xiang, S., Chen, Y., Wei, H., Zhou, Y., Liu, J. & Liu, Y. (2017). *Mater. Des.* **126**, 12–17.
- Long, H., Wei, H., Liu, Y., Mao, S., Zhang, J., Xiang, S., Chen, Y., Gui, W., Li, Q., Zhang, Z. & Han, X. (2016). *Acta Mater.* **120**, 95–107.
- Luo, L., Ai, C., Ma, Y., Li, S., Pei, Y. & Gong, S. (2018). *Mater. Charact.* **142**, 27–38.
- Malamud, F. & Santisteban, J. R. (2016). *J. Appl. Cryst.* **49**, 348–365.
- Nathal, M. V., Mackay, R. A. & Garlick, R. G. (1985). *Mater. Sci. Eng.* **75**, 195–205.
- Nowotnik, A. (2016). *Reference Module in Materials Science and Materials Engineering*, <https://doi.org/10.1016/B978-0-12-803581-8.02574-1>. Amsterdam: Elsevier.
- Pollock, T. M. & Tin, S. (2006). *J. Propul. Power*, **22**, 361–374.
- Pyczak, F., Devirent, B. & Mughrabi, H. (2004). *Superalloys 2004 (Proceedings of the Tenth International Symposium on Superalloys)*, pp. 827–836. Warrendale: TMS.
- Reed, R. C., Tao, T. & Warnken, N. (2009). *Acta Mater.* **57**, 5898–5913.
- Santisteban, J. R. (2005). *J. Appl. Cryst.* **38**, 934–944.
- Stoloff, N. S., Sims, C. T. & Hagel, W. C. (1987). *Superalloys II*. New York: Wiley.
- Strickland, J., Nenchev, B., Tassenberg, K., Perry, S., Sheppard, G., Dong, H., Zhang, R., Burca, G. & D'Souza, N. (2021). *Acta Mater.* **217**, 117180.
- Strickland, J., Tassenberg, K., Sheppard, G., Nenchev, B., Perry, S., Li, J., Dong, H., Burca, G., Kelleher, J. & Irwin, S. (2020). *Sci. Rep.* **10**, 20751.
- Tremsin, A. S. & Vallerga, J. V. (2020). *Radiat. Meas.* **130**, 106228.
- Woracek, R., Santisteban, J., Fedrigo, A. & Strobl, M. (2018). *Nucl. Instrum. Methods Phys. Res. A*, **878**, 141–158.
- Wu, E., Sun, G., Chen, B., Pirling, T., Hughes, D. J., Wang, S. & Zhang, J. (2013). *Acta Mater.* **61**, 2308–2319.
- Zachariasen, W. H. (1945). *Theory of X-ray Diffraction in Crystals*. New York: John Wiley & Sons.
- Zachariasen, W. H. (1969). *Acta Cryst.* **A25**, 102–102.